

A Higher Probability of Detecting Lensed Supermassive Black Hole Binaries by LISA

Zucheng Gao,^{1,2★} Xian Chen,^{1,3†} Yi-Ming Hu,⁴ Jian-Dong Zhang⁴ and Shun-Jia Huang⁴

¹*Astronomy Department, School of Physics, Peking University, Beijing 100871, P. R. China*

²*Institute of Astronomy, University of Cambridge, Madingley Road, Cambridge CB3 0HA, UK*

³*Kavli Institute for Astronomy and Astrophysics at Peking University, Beijing 100871, P. R. China*

⁴*TianQin Research Center for Gravitational Physics and School of Physics and Astronomy, Sun Yat-sen University (Zhuhai Campus), Zhuhai 519082, P. R. China*

Accepted XXX. Received YYY; in original form ZZZ

ABSTRACT

Gravitational lensing of gravitational waves (GWs) is a powerful probe of the matter distribution in the universe. Here we revisit the wave-optics effects induced by dark matter (DM) halos on the GW signals of merging massive black hole binaries (MBHBs), and we study the possibility of discerning these effects using the Laser Interferometer Space Antenna (LISA). In particular, we include the halos in the low-mass range of $10^5 - 10^8 M_\odot$ since they are the most numerous according to the cold DM model. We simulate the lensed signals corresponding to a wide range of impact parameters, and we find distinguishable deviation from the standard best-fit GW templates even when the impact parameter is as large $y \simeq 50$. Consequently, we estimate that over $(0.1 - 1.6)\%$ of the MBHBs in the mass range of $10^{5.0} - 10^{6.5} M_\odot$ and the redshift range of $4 - 10$ should show detectable wave-optics effects. This probability is one order of magnitude higher than that derived in previous works. The uncertainty comes mainly from the mass function of the DM halos. Not detecting any signal during the LISA mission would imply that DM halos with $10^5 - 10^8 M_\odot$ are less numerous than what the cold DM model predicts.

Key words: gravitational waves — gravitational lensing: strong — dark matter

1 INTRODUCTION

Gravitational lensing events are unique probes of the distribution of matter in the universe (Schneider et al. 1992). Like light, gravitational waves (GWs) could also be lensed by intervening matter (Lawrence 1971; Cyrancki 1974; Sonnabend 1979; Marković 1993). The prospect of detecting the lensing of GWs is promising given the increasing number of GW events discovered in the recent years by the Laser Interferometer Gravitational-wave Observatory (LIGO) and the Virgo detectors (Abbott et al. 2016, 2019; Abbott et al. 2020).

One major difference between GW and light is that the former usually has a much longer wavelength. For example, LIGO/Virgo are sensitive to the GWs with a wavelength of $O(10^4)$ km. It is comparable to or longer than the characteristic sizes of many astrophysical objects, such as stars or intermediate-massive black holes (IMBHs). If lensed by these objects, the GWs in the LIGO/Virgo band would behave like light in the wave-optics limit (Ohanian 1974; Bontz & Haugan 1981; Nakamura 1998; Nakamura & Deguchi 1999). In this case, wave diffraction would modify the amplitude and phase of the GWs, producing a characteristic “beating pattern” in the frequency domain of the waveform (Takahashi & Nakamura 2003). In addition, the wave-optics effect could also smear the plane of GW polarization (Cusin & Lagos 2020) and produce beat patterns in the time-domain waveform (Yamamoto 2005; Hou et al. 2020). These effects, in principle, could allow LIGO/Virgo to detect massive stars, IMBHs, and

the dense cores of globular clusters and dark-matter (DM) halos (Moylan et al. 2008; Cao et al. 2014; Takahashi 2017; Christian et al. 2018; Dai et al. 2018; Diego et al. 2019; Jung & Shin 2019; Liao et al. 2019; Meena & Bagla 2020; Oguri & Takahashi 2020; Mishra et al. 2021; Wang et al. 2021). However, so far no strong evidence of lensing effects has been officially reported by LIGO/Virgo (Hannuksela et al. 2019), suggesting that the lensing probability is relatively low.

The Laser Interferometer Space Antenna (LISA) is a future space-based mission aiming at detecting the GWs in the milli-Hertz (mHz) band (Amaro-Seoane et al. 2017). One of its major targets is the merger of two massive black holes (MBHs), preferentially in the mass range of $10^4 \sim 10^7 M_\odot$. Because of the superb sensitivity, LISA could detect MBH mergers up to a redshift of 20 with a signal-to-noise ratio (SNR) as high as $10^2 - 10^3$ (Amaro-Seoane et al. 2017). Such a high redshift suggests that gravitational lensing by the large-scale structure is no longer negligible for LISA (Takahashi 2006; Yoo et al. 2007). The long wavelength and high SNR also indicate that the diffraction effects in the wave-optics limit, which is relatively weak for LIGO/Virgo sources, may become significant for LISA.

For LISA, the lenses which produce the diffraction effects are mainly low-mass dark-matter (DM) halos, as well as the subhalos in massive main halos (Takahashi & Nakamura 2003; Takahashi 2004). Takahashi & Nakamura (2003) considered the DM halos in the mass range of $10^9 \sim 10^{12} M_\odot$ and estimated that the lensing probability for each MBH merger in the LISA band is about $10^{-4} \sim 10^{-3}$. However, the cold DM (CDM) model predicts that the most abundant halos are those in the mass range of $10^6 \sim 10^9 M_\odot$ (e.g. Cooray & Sheth

★ E-mail: phy15gzc@pku.edu.cn

† E-mail: xian.chen@pku.edu.cn

2002; Han et al. 2016). These small halos are not included in the calculation of Takahashi & Nakamura (2003). Moreover, Takahashi & Nakamura (2003) imposed a maximum impact parameter $y = 3$ for the sources, to ensure a strong, detectable diffraction effect. This criterion, however, may be too strict. The high SNR of LISA sources would enable us to detect weak lensing signals even when the impact parameter is larger. Since the lensing probability increases with y^2 , previous studies could have significantly underestimated the detection rate of lensed signals.

To elucidate the real detection rate, we revisit the signals of the lensed MBHs in the LISA band. We pay special attention to the events with large impact parameters and we employ the matched-filtering technique to search for weak wave-optics effects in the signal. We also improve the lens model by including the halos and subhalos at the lower mass end. We remark that although the calculation is based on LISA, the conclusion also applies to space-borne GW missions with slightly different frequency coverage, such as TianQin (Mei et al. 2020). The paper is organized as follows. In Section 2, we describe our method, including the calculation of the lensing signal in the wave-optics limit, the mass function of halos and subhalos, the probability of lensing, as well as the matched-filtering technique. Then in Section 3 we quantify the difference between the lensed and unlensed signals and derive a criterion for detecting the diffraction effect. Using this criterion, we estimate the lensing probability for the MBH mergers in the LISA band in Section 4. We discuss the importance of DM models in Section 5 and conclude in Section 6. Throughout the paper, we assume a flat Λ CDM cosmology with the parameters $\Omega_m = 0.27$, $\Omega_\Lambda = 0.73$, $H_0 = 72 \text{ km s}^{-1} \text{ Mpc}^{-1}$, $\sigma_8 = 0.9$. Therefore, in our work $h := H_0 / (100 \text{ km s}^{-1} \text{ Mpc}^{-1}) = 0.72$.

2 METHOD

2.1 Lensing Model

For simplicity, we assume a singular isothermal sphere (SIS) profile for our DM halos and subhalos. In this case, we can follow Takahashi & Nakamura (2003) to model the diffraction of GWs. Using a more realistic Navarro-Frenk-White (NFW) profile usually leads to a slightly smaller magnification factor (Takahashi & Nakamura 2003; Gil Choi et al. 2021).

The basic picture of lensing of GWs is illustrated in Figure 1, where D_L , D_S , and D_{LS} denote the angular diameter distances to the lens, to the source, and their difference. All these quantities are measured in the frame of the observer.

The magnification factor is defined as

$$F(\omega, \boldsymbol{\eta}) := \frac{\tilde{\phi}_{obs}^L(\omega, \boldsymbol{\eta})}{\tilde{\phi}_{obs}(\omega, \boldsymbol{\eta})}, \quad (1)$$

where $\tilde{\phi}_{obs}^L(\omega, \boldsymbol{\eta})$ and $\tilde{\phi}_{obs}(\omega, \boldsymbol{\eta})$ are the lensed and unlensed gravitational wave amplitudes in the Fourier space, ω is the observed angular frequency of the GW, and $\boldsymbol{\eta}$ is the position vector on the source plane (“impact parameter” hereafter). Taking the cosmological redshift into account, the magnification factor can be calculated with

$$F(\omega, \boldsymbol{\eta}) = \frac{\omega(1+z_L)D_S}{2\pi i D_L D_{LS}} \int d^2\xi \exp[i\omega(1+z_L)t_d(\boldsymbol{\xi}, \boldsymbol{\eta})], \quad (2)$$

where z_L is the redshift of the lens and t_d is the time delay caused by lensing. The time delay can be computed with

$$t_d(\boldsymbol{\xi}, \boldsymbol{\eta}) = \frac{D_L D_S}{2D_{LS}} \left| \frac{\boldsymbol{\xi}}{D_L} - \frac{\boldsymbol{\eta}}{D_S} \right|^2 - \hat{\psi}(\boldsymbol{\xi}) + \hat{\phi}_m(\boldsymbol{\eta}), \quad (3)$$

where $\hat{\phi}_m(\boldsymbol{\eta})$ denotes the arrival time of the unlensed GW, which is

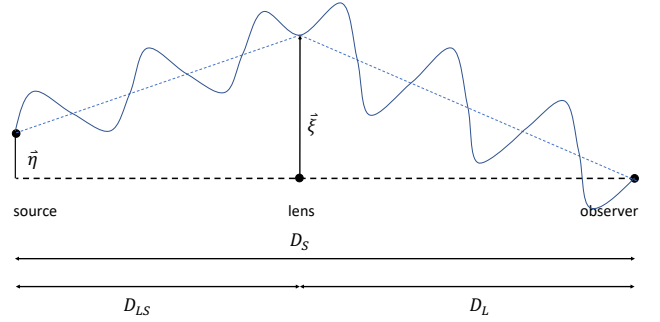


Figure 1. Physical picture of GW lensing. The vectors $\boldsymbol{\eta}$ and $\boldsymbol{\xi}$ denote the two positions on the source plane and on the lens plane. For illustrative purposes the two vectors are aligned but in principle they are not. The angular diameter distances D_L , D_S , and D_{LS} are measured in the rest frame of the observer.

approximately $D_S [1 + |\boldsymbol{\eta}/D_S|^2/2]/c$, and $\hat{\psi}$ is the deflection potential which solves the equation

$$\nabla_{\boldsymbol{\xi}}^2 \hat{\psi}(\boldsymbol{\xi}) = 8\pi \Sigma(\boldsymbol{\xi}), \quad (4)$$

with $\nabla_{\boldsymbol{\xi}}^2$ the two-dimensional Laplacian and $\Sigma(\boldsymbol{\xi})$ the mass surface density of the lens.

For the purpose of numerical calculation, we define the dimensionless positions as

$$\mathbf{x} = \frac{\boldsymbol{\xi}}{\xi_0}; \quad \mathbf{y} = \frac{D_L}{\xi_0 D_S} \boldsymbol{\eta}, \quad (5)$$

where ξ_0 is the Einstein radius. In the SIS model, it can be calculated with $\xi_0 = 4\pi\sigma_v^2 D_L D_{LS} / c^2 D_S$, where σ_v is the velocity dispersion of the lens. The corresponding dimensionless frequency is

$$w = 4GM_L(1+z_L)\omega/c^3, \quad (6)$$

where M_L is the so-called “lens mass”, which is defined as the mass enclosed by a circle of the Einstein radius in the lens plane. In the SIS model, we have $M_L = 4\pi^2\sigma_v^4 D_L D_{LS} / (GD_S c^2)$ (Appendix A). Using the above nondimensional quantities, the time delay can be rewritten as

$$\begin{aligned} T(\mathbf{x}, \mathbf{y}) &= \frac{D_L D_{LS}}{D_S} \xi_0^{-2} t_d(\boldsymbol{\xi}, \boldsymbol{\eta}) \\ &= \frac{1}{2} |\mathbf{x} - \mathbf{y}|^2 - \frac{D_L D_{LS}}{D_S} \xi_0^{-2} \hat{\psi}(\boldsymbol{\xi}) + \frac{D_L D_{LS}}{D_S} \xi_0^{-2} \hat{\phi}_m(\boldsymbol{\eta}). \end{aligned} \quad (7)$$

It follows that the nondimensional amplification factor is

$$F(w, \mathbf{y}) = \frac{w}{2\pi i} \int d^2x \exp[iwT(\mathbf{x}, \mathbf{y})]. \quad (8)$$

In the SIS model the last equation can be calculated with

$$\begin{aligned} F(w, \mathbf{y}) &= -iwe^{iwy^2/2} \int_0^\infty dx x J_0(wxy) \times \\ &\quad \exp[iw(\frac{1}{2}x^2 - x + \phi_m(y))], \end{aligned} \quad (9)$$

where $\phi_m(y) = y + 1/2$ and J_0 is the zeroth-order Bessel function. The corresponding amplification factor $|F|$ and phase-change factor θ_F are

$$|F| = \sqrt{FF^*}, \quad \theta_F = -i \ln[F/F^*], \quad (10)$$

where F^* is the complex conjugate of F .

Figure 2 shows the dependence of $|F|$ and θ_F on the dimensionless

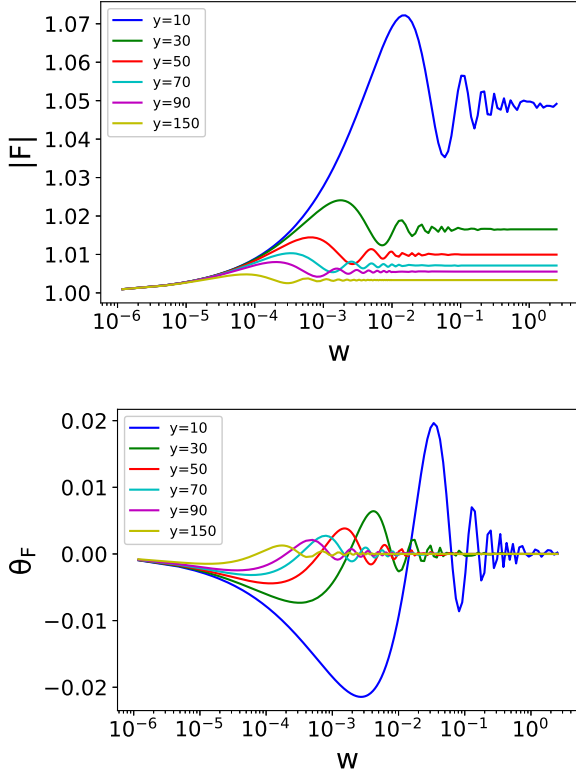


Figure 2. The amplification factor (upper panel) and the phase-change factor (lower panel) as a function of the dimensionless frequency according to the SIS model. Different lines correspond to different impact parameters (y). Note that this is only a demonstration of some selected amplification factors. We also calculate the same quantities for $y = 1, 5, 20, 40, 60, 80, 100$.

frequency w and impact factor y . We notice three results which are important for the later estimation of the lensing probability.

First, the amplification factor $|F|$ in general decreases with increasing impact parameter y . However, even when y is relatively large, e.g., $y = 90$, the amplification factor converges to the value in the geometric limit and is not 1, and the phase-change factor does not vanish. The implication is that even though the wave-optics effect is weak, it may still be detectable if the SNR of the event is sufficiently large. We will study the criterion for detecting such a weak signal in the later sections. The previous works, however, normally adopt an upper limit between $y = 1$ and 10 to estimate the lensing probability (e.g., Takahashi & Nakamura 2003). Such a small value could cause an underestimation of the number of lensing events.

Second, when y is fixed, both $|F|$ and θ_F could vary significantly due to the change of w . In particular, the critical value of y , above which the diffraction effect becomes undetectable, depends on w , which, according to Equation (6), depends on the lens mass, lens redshift, and the GW frequency. We will take such a dependence into account in the following sections. These results indicate that it is oversimplified to use a single value of y to estimate the lensing probability in the diffraction limit, as is often the case in the previous works.

Third, the peaks of the amplification factor and the phase-change angles shift to smaller w as y increases. As a result, for large impact parameters, i.e., $y = 10 - 150$, the wave-optics effect appears the most significant at a small value of frequency, e.g., $w \sim (10^{-5} - 10^{-3})$. Such a small dimensionless frequency corresponds to a low-mass

lens according to Equation (6), which is about

$$M_L(1+z_L) \approx 800 M_\odot \left(\frac{w}{10^{-4}} \right) \left(\frac{f}{10^{-3} \text{Hz}} \right)^{-1}. \quad (11)$$

The corresponding halo mass is also small, about $10^5 - 10^7 M_\odot$ according to Appendix A. The above relationships suggest that the majority of the diffraction events detected by LISA should be induced by small halos, because (i) the lensing probability increases with y^2 and (ii) when y is large only small halos produce strong diffraction effect.

2.2 DM Halos and Subhalos

The lenses of our interest are those DM halos as small as $10^5 - 10^7 M_\odot$. The last section has shown that they induce an observable diffraction effect to the mHz GWs in the LISA band. Two types of DM halos fall in this mass range.

The first type reside in the low-density regions of the universe. They predominate the low-mass end of the mass function of ordinary DM halos (e.g. Wang et al. 2020). To compute the number density of these halos, we adopt the Sheth Tormen halo mass function dn/dM_h (see Cooray & Sheth 2002, for a review), where n denotes the number density of halos in unit of Mpc^{-3} and M_h is the halo mass. Note that by convention dn/dM_h has a unit of $\text{M}_\odot^{-1} \text{Mpc}^{-3} \text{h}^3$.

The second type of DM halos fall in our interested mass range are the substructures of those massive DM halos. These substructures are often referred to as “subhalos”. Numerical simulations show that given the mass M_h of a main halo, the masses of the subhalos follow a power-law distribution with a universal power-law index (e.g. Gao et al. 2004a,b; Diemand et al. 2004; Libeskind et al. 2005; Giocoli et al. 2008)). Following Han et al. (2016), we write the mass function of the subhalos as

$$\frac{dN(<R)}{d \ln m} = A(R) \frac{M(<R)}{m_0} \left[\frac{m}{m_0} \right]^{-\alpha}, \quad (12)$$

where $N(<R)$ is the number of subhalos within a radius of R of the main halo, m is the mass of the subhalo, $A(R)$ is a normalization factor, $M(<R)$ is the total mass enclosed by the radius R , and $m_0 = 10^{10} M_\odot$ and $\alpha = 0.96$ are constants nearly independent of the halo mass or redshift. In the later calculation, we are mainly interested in the number of subhalos within the virial radius R_{vir} of the main halo, regardless of their spatial distribution within the main halo. Therefore, we should replace R with R_{vir} when using Equation (12). By construction, the total mass within the virial radius is $M(<R_{\text{vir}}) = M_h$. This leaves $A(R_{\text{vir}})$ the only quantity that is undetermined. We notice that Figure 15 of Han et al. (2016) gives the value of $A(<R)$ which shows that at $R = R_{\text{vir}}$ the value converges to 0.01 for a wide range of halo mass, from $M_h = 10^{12} h^{-1} M_\odot$ to $10^{15} h^{-1} M_\odot$. For this reason, we adopt $A(<R_{\text{vir}}) = 0.01$ for our later calculations.

Knowing the mass function of subhalos in one main halo, we can calculate the mass function density at a given redshift for all the subhalos of the same mass with

$$\frac{dn_{\text{sub}}}{dm}(m, z_L) = \int dM'_h \frac{dn(M'_h, z_L)}{dM'_h} \frac{dN}{d \ln m} \frac{1}{m}. \quad (13)$$

Such a quantity is useful for our later calculation of the lensing probability. Correspondingly, the total mass function density contributed by the halos and subhalos of a mass of M_h is

$$\xi_{\text{lens}}(M_h, z) = \frac{dn_{\text{sub}}}{dM_h}(M_h, z) + \frac{dn}{dM_h}(M_h, z). \quad (14)$$

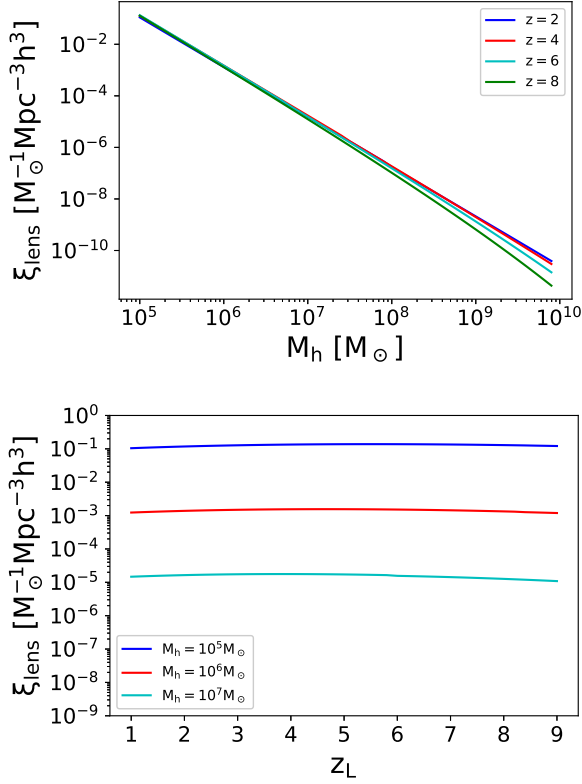


Figure 3. The mass function of the small halos which could produce diffraction effects as a function the halo mass (upper panel) or redshift (lower panel).

Note that to find the lens mass M_L corresponding to a halo mass M_h , the relationship derived in Appendix A is applied.

Figure 3 shows the mass function density predicted by Equation (14). We can see that the mass function density has little evolution from redshift $z = 2$ to 6 (upper panel), and it is more sensitive to the halo mass (lower panel). We note that in general halos are more numerous than subhalos. Nevertheless, we include subhalos in the calculation for completeness.

2.3 Calculation of the Lensing Probability

To calculate the lensing probability, we have to specify (i) the number of lenses of different masses at each redshift and (ii) the solid angle these lenses cover in which we can detect the diffraction of GW.

For (i), we start with the halo mass function density derived in the previous section, $\xi_{\text{lens}}(M_h, z)$. Since the SIS model predicts a unique relationship between the lens mass and halo mass, $M_h(M_L, z_L, z_S)$ (see Appendix A), we can rewrite ξ_{lens} as a function of the lens mass, i.e., $\xi_{\text{lens}}(M_h(M_L, z_L, z_S), z_L)$. Using this new mass function, we can calculate the number of lens in the mass range $(M_L, M_L + dM_L)$ and redshift bin $(z_L, z_L + dz_L)$ per unit solid angle using the equation

$$\frac{d^3 N_{\text{lens}}(M_L, z_L, z_S)}{dM_L dz_L d\Omega} = \xi_{\text{lens}}(M_h(M_L, z_L, z_S), z_L) \times \chi^2(z_L) \frac{d\chi}{dz} \frac{dM_h}{dM_L}, \quad (15)$$

where $\chi(z)$ is the comoving distance for redshift z .

Figure 4 shows the result of Equation (15) integrated over a redshift range of $[0, z_{L\text{max}}]$ and above a certain lens mass. The source is assumed to be at $z_S = 4$. It is clear that the number of lenses in

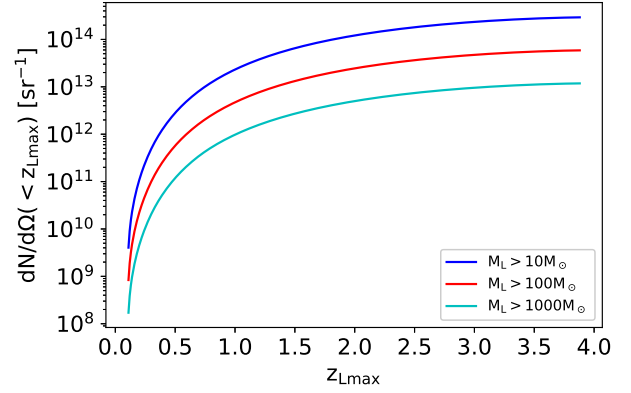


Figure 4. Cumulative distribution of lenses per unit solid angle. The three curves from top to bottom are counting the lenses above three different minimum masses, i.e., $M_{L\text{min}} = (10, 100, 1000) M_\odot$. In this example, the source is at $z_S = 4$.

a solid angle increases with redshift, and small lenses (e.g., $M_L \sim 10 M_\odot$) are the most numerous. Therefore, we expect that small halos contribute most of the lensing events. We have considered the lenses as small as $10 M_\odot$ because they correspond to a halo mass of about $10^5 M_\odot$ (see Appendix A).

As for (ii), suppose y_{crit} is the critical impact parameter in the source plane within which the effect due to the diffraction of GW is detectable. In the lens plane, the critical impact parameter corresponds to an angular size of

$$\theta(M_S, M_L, z_L, z_S) = \xi_0 y_{\text{crit}} / D_L. \quad (16)$$

We have written θ as a function of the source mass M_S and redshift z_S to highlight the dependence of y_{crit} on the “loudness” of the source. Therefore, the lensing effect is detectable within a solid angle of

$$\pi\theta^2 = \pi y^2 \times \frac{4GM_L D_{LS}}{c^2 D_L D_S} \quad (17)$$

towards the lens, where we have used the relation

$$\xi_0 = 2\sqrt{GM_L \frac{D_L D_{LS}}{c^2 D_S}} \quad (18)$$

from the SIS model. Summing up all possible lenses between the source and the observer, we derive the lensing probability—the probability of detecting the diffraction effect in a given GW source—as

$$P = \int_0^{z_S} dz_L \int \pi\theta^2 \times \frac{d^3 N_{\text{lens}}(M_L, z_L, z_S)}{dM_L dz_L d\Omega} dM_L. \quad (19)$$

In principle, the integration should be performed over all possible lens masses. In practice, we restrict the integration within a mass range $[M_{L\text{min}}, M_{L\text{max}}]$. The upper and lower limits are functions of lens redshift z_L , which should be determined by evaluating the prominence of the diffraction effect. Only those lenses producing a detectable diffraction effect should be counted. The following subsection explains how we quantify the detectability of the diffraction effect.

2.4 Signal and Matched Filtering

The magnification factor derived in Section 2.1 is a function of GW frequency. To use it, we need to first derive the unlensed GW signal

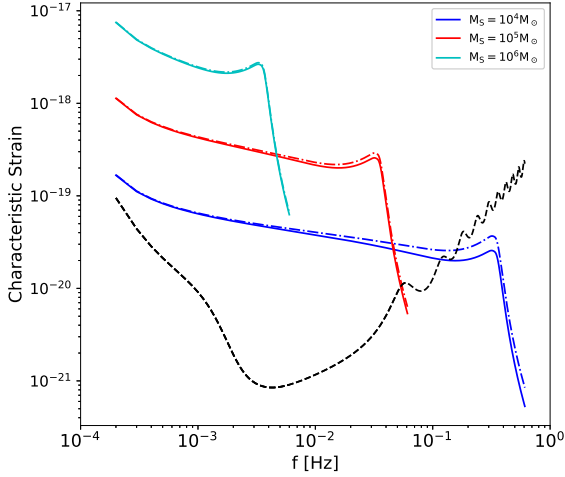


Figure 5. Characteristic strains of unlensed (solid lines) and lensed (dot-dashed lines) MBH binaries. The lines of different colors correspond to different total masses of the binaries. The black dashed line is the square root of the spectral noise density of LISA, i.e., $\sqrt{f S_h(f)}$, adopted from Robson et al. (2019).

in the frequency domain. This is done by a Fourier transformation,

$$\tilde{h}(f) = \int e^{2\pi i f t} h(t) dt, \quad (20)$$

of the GW strain $h(t)$ in the time domain.

For illustrative purposes, we show in Figure 5 the characteristic strain of three MBH mergers (solid curves). We assume equal-mass mergers with zero eccentricity, zero spins and zero inclination for simplicity and the total masses are $M_S = 10^4, 10^5$, and $10^6 M_\odot$ respectively. The source redshift is fixed at $z_S = 4$ in these examples. The waveforms are generated using the “IMRPhenomC” model in the PyCBC package (Santamaría et al. 2010; Nitz et al. 2020), excluding the effect of BH spin. As is mentioned in Dai et al. (2018), spin and eccentricity could also introduce diffraction-like waveform modulation. However, they also found that for misaligned spin, the induced pattern is more densely packed at low frequencies while the diffraction effect is spread across the frequency domain. The amplitude modulation due to spin is also much higher than its phase modulation, which is distinctive from the diffraction effect. As for eccentricity, it induces high harmonics, which is a feature absence from diffraction effect. Based on these differences, we assume that the modulation of the waveform by spin and eccentricity can be modeled in the future. Here we focus only on the diffraction effect. For the following calculation of unlensed template, we only vary the M_S and z_S parameters. Because we assume circular orbits for the MBH binaries, the merger time is about $1.7 f_{\text{mHz}}^{-8/3} M_4^{-5/3} (1+z_S)$ years (Peters & Mathews 1963), where f_{mHz} is the GW frequency in unit of mHz and M_4 is the total BH mass in unit of $10^4 M_\odot$. It is shorter than the canonical lifetime of LISA (5 years) except in the case of the smallest BHs.

We now integrate the characteristic strain in Figure 5 to derive the SNR of each merger. The calculation takes advantage of an inner product (Finn 1992; Cutler & Flanagan 1994) which is defined as

$$\langle h_1 | h_2 \rangle = 2 \int_0^\infty \frac{\tilde{h}_1^*(f) \tilde{h}_2(f) + \tilde{h}_1(f) \tilde{h}_2^*(f)}{S_h(f)} df, \quad (21)$$

where h_1 and h_2 are two waveforms, $S_h(f)$ is the one-sided power spectral density for LISA (from Robson et al. 2019), and the star

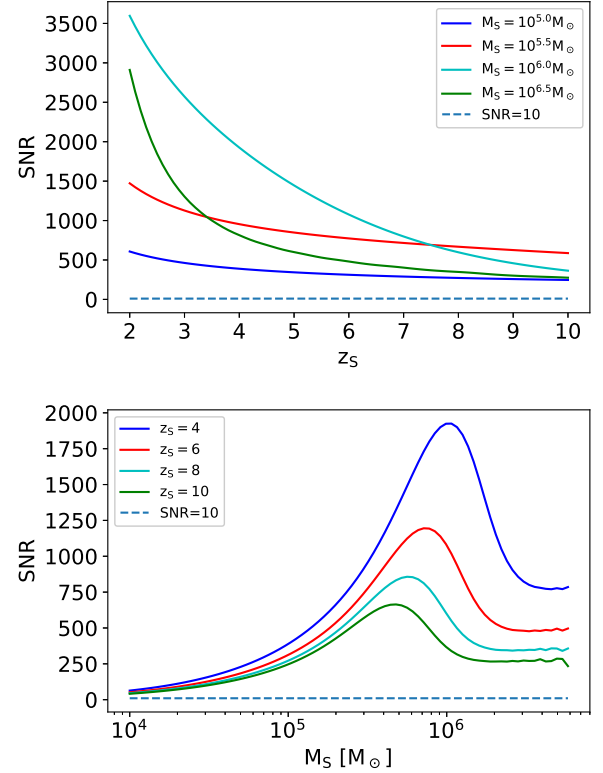


Figure 6. SNR as a function of the redshift (upper panel) or the total mass (lower panel) of the source.

symbols denote the complex conjugates. The SNR of a signal h is defined as $\text{SNR} := \sqrt{\langle h | h \rangle}$.

Figure 6 shows the SNR of different MBH mergers at different redshift. We see that when the total mass is higher than about $10^4 M_\odot$ and the source redshift is lower than 10, the source in general has a SNR much higher than 10. These events are detectable by LISA (Amaro-Seoane et al. 2017). In the following we study the lensing signals of these events.

The strain of the lensed signals are shown in Figure 5 as the dot-dashed lines. In the calculation, we assumed that the lens has a mass of $M_L = 10^4 M_\odot$ and is at a redshift of $z_L = 2$. The impact parameter is set to $y = 1$ to maximize the effect in these examples. In this case, we can discern by eye that the lensed signals differ from the unlensed ones.

In more general cases, the impact parameters are much larger than 1 so that the diffraction effects are much more difficult to discern by eye (e.g., see Figure 2). Therefore, we employed the matched-filtering technique to quantify the deviation of a lensed signal from a waveform in the template bank. Suppose h_1 is the lensed signal and h_2 is an unlensed template, the difference $\delta h := h_1 - h_2$ is discernible when the SNR of the difference is larger than 1, i.e., $\langle \delta h | \delta h \rangle > 1$ (see Lindblom et al. 2008, for a proof).

In our work, h_2 , the unlensed waveform, is generated from the aforementioned PyCBC package. We explore the parameter space of the template bank until we find the minimum value of $\langle \delta h | \delta h \rangle$. If this minimum $\langle \delta h | \delta h \rangle$ is still greater than 1, we deem the lensing signal detected. We call the corresponding waveform the “best fit”. Note that the best-fit MBH binaries may differ from the real ones because of lensing.

We are being optimistic in adopting this criterion because we

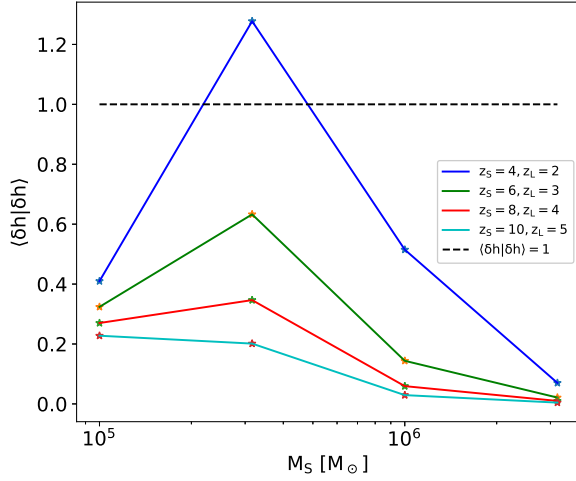


Figure 7. The inner product $\langle \delta h | \delta h \rangle$ as a function of the total mass of the source. The solid lines of difference colors correspond to different combinations of source redshift, and lens redshift. In this example, the lens mass is set to $M_L = 16 M_\odot$ and the impact parameter to $y = 40$. The black dashed line marks the place where $\langle \delta h | \delta h \rangle = 1$.

assume that the deviation of the waveform from the theoretical waveform comes completely from the lensing effect. However, when the SNR is high, the criterion can be satisfied due to other factors, such as the presence of other signals, inaccurate waveform template, and the non-Gaussianity/non-stationarity of the noise. Nevertheless, it provides a practical criterion by which we can select from our simulations the lensing events which contain possibly discernible diffraction features.

3 DIFFERENCE BETWEEN THE LENSED AND THE BEST-FIT WAVEFORMS

The significance of the diffraction effect on the lensing signal depends on five parameters. Two of them are related to the source, i.e., the total mass of the MBH binary M_S and the source redshift z_S . Two are related to the lens, i.e., the lens mass M_L and redshift z_L . The final one is the impact parameter y . In this section, we choose a grid of typical values for these five parameters and we investigate how the variation of their values affects $\langle \delta h | \delta h \rangle$. More specifically, we choose $M_S = (10^{5.0}, 10^{5.5}, 10^{6.0}, 10^{6.5}) M_\odot$; $M_L = (16, 80, 160, 800, 1600, 8000, 16000) M_\odot$; $z_S = (4, 6, 8, 10)$. The value of z_L depends on z_S and we choose $z_L = (0, 1/5, 2/5, 3/5, 4/5)z_S$ unless mentioned otherwise.

Figure 7 shows the dependence of $\langle \delta h | \delta h \rangle$ on the source mass M_S . Comparing it with the lower panel of Figure 6, we find that the inner product behaves similarly as the SNR of the unlensed signal. The reason is that higher SNR normally makes the deviation between the lensed signal and the best-fit template more discernible.

The dependence of $\langle \delta h | \delta h \rangle$ on the lens mass M_L is shown in Figure 8. In this example with a high impact parameter $y = 40$, we find that $\langle \delta h | \delta h \rangle$ first increase and then decrease with the lens mass. The peak corresponds to a lens whose Einstein radius is comparable to the wavelength of the GW. We can also understand the result through the dimensionless frequency w and the corresponding amplification factor. On one hand, when M_L is small, w is small. According to Figure 2, the lensing effect is small. On the other hand, when M_L is particularly large so that w approaches unity, the system enters the

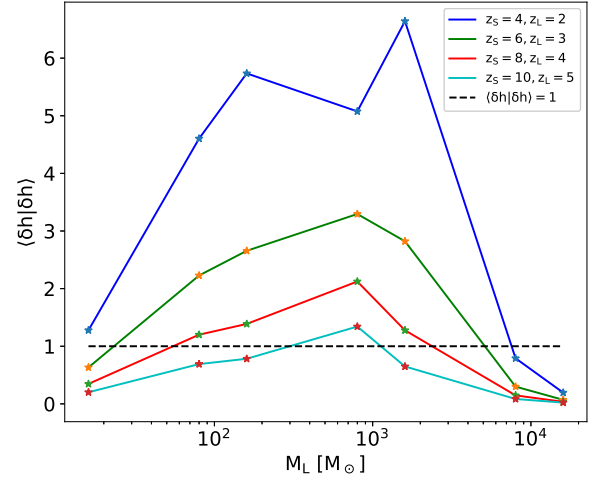


Figure 8. The same as Fig. 7 but varying the lens mass M_L while fixing the source mass at $M_S = 10^{5.5} M_\odot$. The impact parameter is fixed at $y = 40$ for easier comparison.

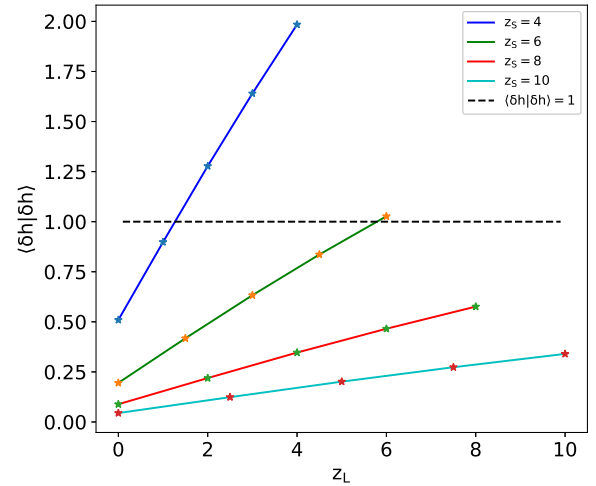


Figure 9. Dependence of the inner product $\langle \delta h | \delta h \rangle$ on the lens redshift z_L . In this example, the source mass is chosen to be $M_S = 10^{5.5} M_\odot$ and the lens mass is $M_L = 16 M_\odot$. The impact parameter is fixed at $y = 40$ for easier comparison.

geometric-optics regime where at any frequency the GW is amplified by the same factor $\sqrt{1 + 1/y}$. The wave-optics effect, which is a frequency-dependent amplification of GWs, diminishes in this case.

Figure 9 shows the inner product as a function of the lens redshift. We find that $\langle \delta h | \delta h \rangle$ increases as the lens redshift approaches the source redshift. This behavior is caused by the fact that the lensing effect is in general stronger when the lens and the source are closer. We also find that the sources at higher redshift in general produce a smaller $\langle \delta h | \delta h \rangle$. This result stems from the decrease of the SNR as the source redshift increases. Note that the effect of lens redshift should be similar, but relatively weak, compared to the effect induced by the lens mass. This is because they affect w through the product $(1 + z_L)M_L$. While z_L can only vary by a factor of a few, M_L can change by orders of magnitude.

Finally, we show the dependence of $\langle \delta h | \delta h \rangle$ on the impact pa-

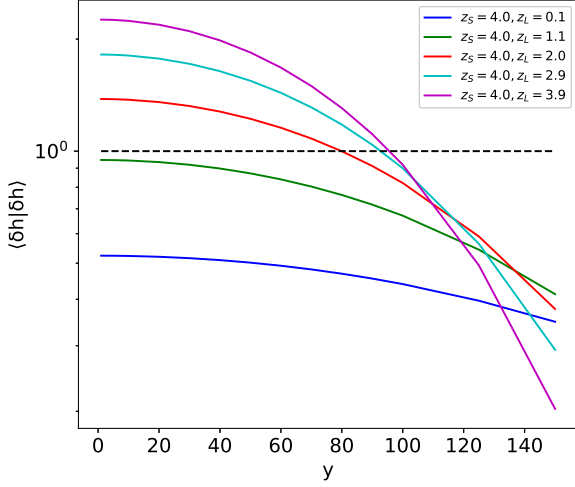


Figure 10. The inner-product $\langle \delta h | \delta h \rangle$ as a function of the dimensionless impact parameter y . These examples assume $M_S = 10^{5.5} M_\odot$ and $M_L = 16 M_\odot$.

parameter y in Figure 10. In general, the inner product decreases with the impact parameter. Their intersection with the horizontal line $\langle \delta h | \delta h \rangle = 1$ determines y_{crit} . We can see that, for some parameters, y_{crit} can be as large as 10^2 . Such a large impact parameter has not been accounted for in the previous studies of the wave-optics effect. It could significantly enhance the lensing probability of LISA MBHs.

4 LENSING PROBABILITY

Having investigated the dependence of the inner product $\langle \delta h | \delta h \rangle$ on the parameters M_S , z_S , M_L , z_L , and y , we can now include the halo mass function and calculate the probability that a MBH binary in the LISA band has $\langle \delta h | \delta h \rangle > 1$ due to the diffraction effect. We denote this probability as $P(\langle \delta h | \delta h \rangle > 1)$, and the expression can be derived from Equation (19).

Given (M_S, z_S, M_L, z_L) , we first calculate the critical impact parameter y_{crit} which produces exactly $\langle \delta h | \delta h \rangle = 1$. Figure 11 shows the critical impact parameter as a function of the lens redshift and lens mass. In these examples, we have chosen $M_S = 10^{5.5} M_\odot$ and varied z_S . We can see that in a large redshift range, y_{crit} has a value above 40, much higher than the value of $y_{\text{crit}} = 3$ as has been chosen by the previous studies (e.g. Takahashi & Nakamura 2003). Moreover, sources at lower redshifts have higher y_{crit} , since the higher SNR makes it easier to discern the wave-optics effect. In this work we have calculated the y_{crit} for a total number of $4 \times 7 \times 4 \times 5 = 560$ grid points, covering the four-dimensional parameter space of (M_S, z_S, M_L, z_L) . Then by interpolation, we construct the function $y_{\text{crit}}(M_S, z_S, M_L, z_L)$ which we will use in the following calculation of the lensing probability.

To calculate the probability, we replace θ in the integrand of Equation (19) with $\theta(y_{\text{crit}})$ (given by Equation (17)) and integrate to give the probability $P(y < y_{\text{crit}})$. This probability $P(y < y_{\text{crit}})$ is equivalent to $P(\langle \delta h | \delta h \rangle > 1)$. In principle, given the source, i.e., after fixing M_S and z_S , the y_{crit} in the integrand is a function of both z_L and M_L . In practice, we only consider the lenses more massive than $M_L = 16 M_\odot$ because less massive lenses in general do not produce a sufficiently large inner product $\langle \delta h | \delta h \rangle$, as Figure 8 has shown.

The resulting lensing probabilities are given in Table 1. We find

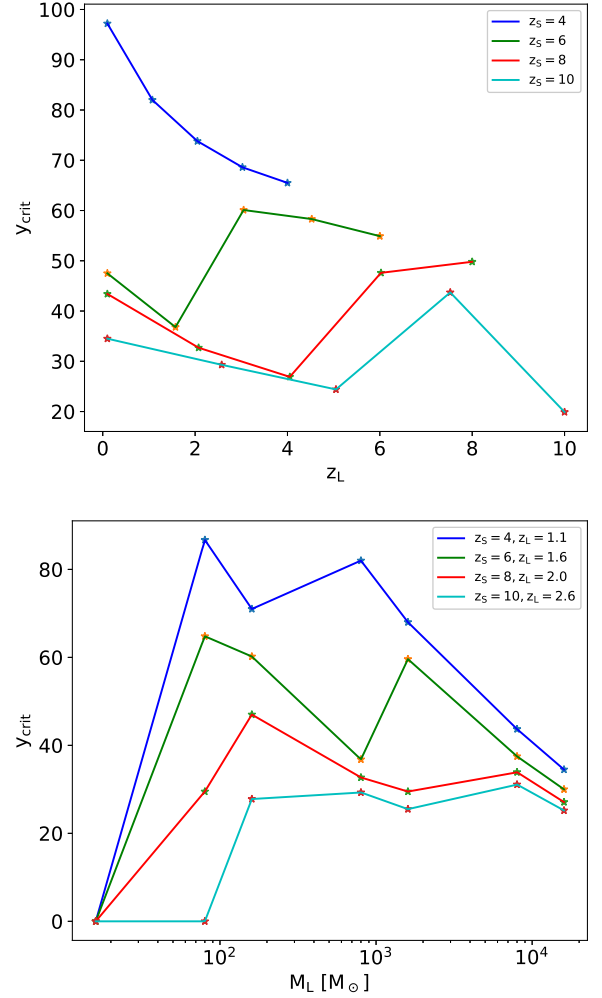


Figure 11. The critical impact parameter which gives $\langle \delta h | \delta h \rangle = 1$ as a function of the lens redshift (upper panel) or lens mass (lower panel). Different lines correspond to different source redshift. In the upper panel, we fixed $M_S = 10^{5.5} M_\odot$ and $M_L = 800 M_\odot$, while in the lower one we fixed $M_S = 10^{5.5} M_\odot$.

that, in general, the probability of detecting the wave-optics effect is about $(0.1 - 1.6)\%$. Although low, such a probability is one order of magnitude larger than that those found in Takahashi & Nakamura (2003). The enhancement is influenced by a combination of larger impact parameters and more numerous lenses, but also the decrease of lens mass, which we will discuss in detail in the next section. We note that the probabilities $P(M_S, z_S)$ derived here can be used to estimate the number of MBH mergers which show wave-optics effects prominent enough to be detectable by LISA, once the merger rate of MBHs as a function of mass (M_S) and redshift (z_S) is known.

In this work, we did not consider a lens mass higher than $1.6 \times 10^4 M_\odot$ because such lenses contribute a small fraction (less than 10%) to the total probability. The reasons are two fold. (i) The corresponding halos mass is greater than $10^8 M_\odot$. The number density of such halos is low. (ii) As the lens mass exceeds $1.6 \times 10^4 M_\odot$, the lensing effect will approach the geometric limit, diminishing the detectability of the diffraction effect.

Table 1. Total Lensing Probability for Different Source Parameters

$P(M_S, z_S)$	$M_S = 10^{5.0} M_\odot$	$M_S = 10^{5.5} M_\odot$	$M_S = 10^{6.0} M_\odot$	$M_S = 10^{6.5} M_\odot$
$z_S = 4$	0.0038	0.012	0.016	0.0059
$z_S = 6$	0.0050	0.014	0.0081	0.0024
$z_S = 8$	0.0059	0.012	0.0056	0.00095
$z_S = 10$	0.0057	0.0094	0.0036	0.00040

5 IMPACT OF DM MODELS

We notice that [Takahashi & Nakamura \(2003\)](#) derived a lensing probability of $10^{-4} \sim 10^{-3}$ for the MBH binaries in the LISA band. It is at least one order of magnitude smaller than our estimation. The discrepancy stems from the different ranges of lens mass adopted in these two works.

[Takahashi & Nakamura \(2003\)](#) considered the lenses in the mass range of $M_L = 10^6 \sim 10^9 M_\odot$, which corresponds to a halo mass of $10^9 \sim 10^{12} M_\odot$. Such lenses are already in the geometric-optics limit. Moreover, they assumed a critical impact parameter of $y_{\text{crit}} = 3$. In our model, we considered the lenses in the mass range of $1.6 \times 10^1 \sim 1.6 \times 10^4 M_\odot$. The corresponding halo mass is $10^5 \sim 10^8 M_\odot$. These lenses produce wave-optics effect in the lensing signal, and we have shown that the effect is detectable even for a large impact parameter of $y \sim 40$ (Figure 11).

The difference of the lens masses affects the lensing probability in two ways. (i) In our model, the solid angle within in which the lensing signal is detectable is about 100 times smaller than the choice of [Takahashi & Nakamura \(2003\)](#) (assuming $y_{\text{crit}} = 40$), since it is proportional to $y_{\text{crit}}^2 M_L$ according to Equation (17). (ii) Our lenses are about 1000 times more numerous than those considered in [Takahashi & Nakamura \(2003\)](#) according to Figure 3. Combining these two consequences, we find that our lensing probability is about 10 times higher than that derived in [Takahashi & Nakamura \(2003\)](#). The case of higher mass source at $z_S = 10$ is somewhat different, because the SNR reduces significantly. Consequently, y_{crit} decreases, so that the probability is only several times larger than what [Takahashi & Nakamura \(2003\)](#) has derived.

The above comparison suggests that the lensing probability is sensitive to the abundance of small halos. Since different DM models predict very different number density for small halos, we now investigate the dependence of the lensing probability on the lower boundary of the halo mass function. To simulate the effect of different DM models, we cut off the integration of Equation (19) at different lower boundaries M_{hmin} and count only those halo with $M_h > M_{\text{hmin}}$. The result is shown in Figure 13. We see a sharp cut off around $M_{\text{hmin}} = 10^8 M_\odot$. Compared to [Takahashi & Nakamura \(2003\)](#), our result indicates that the probability of detecting the diffraction effect of a MBH binary in the LISA band is significantly enhanced, because of the numerous small halos in the CDM paradigm. It also implies that if warm DM predominates (e.g. [Lovell et al. 2014](#)), the probability of detecting the wave-optics effect would be low.

6 SUMMARY CONCLUSION

In this work, we studied the lensing signals of the MBH binaries in the LISA band. We focused on the wave-optics effect and found that it is produced mainly by the DM halos and subhalos in the mass range of $10^5 \sim 10^8 M_\odot$. Using the matched-filtering technique, we showed that the effect could be discernible by LISA even when the

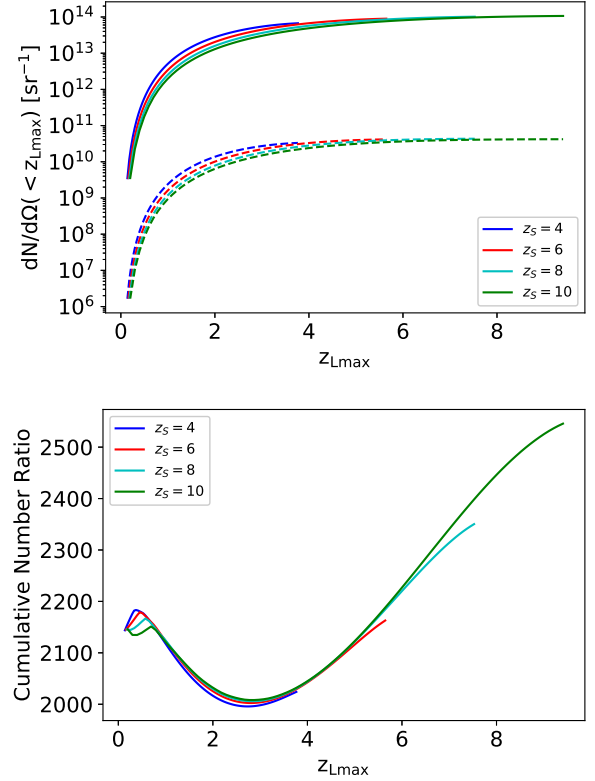


Figure 12. Upper panel: Cumulative distribution of the number of lenses as a function of the upper limit of lens redshift $z_{L\max}$. The solid lines represent the lenses in the mass range of $M_L = 16 \sim 1.6 \times 10^4 M_\odot$, while the dashed one represent the lenses of $10^6 \sim 10^9 M_\odot$. The four colors refer to four different source redshifts. Lower panel: The ratio between the two kinds of cumulative lens numbers.

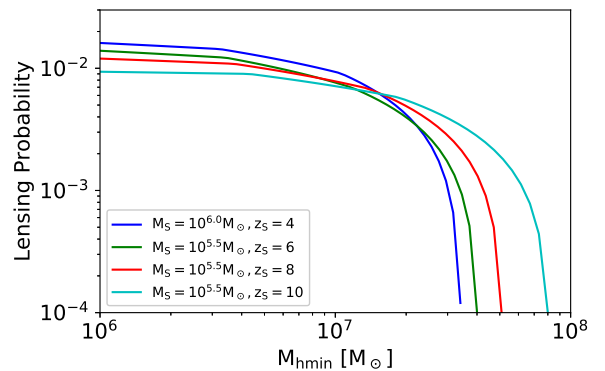


Figure 13. The total lensing probability as a function of the minimum halo mass. Different colors refer to difference source mass and redshift.

source has an impact parameter as large as $y = 40$, or even $y = 100$ in some cases. Such a large impact parameter substantially enhances the probability of detecting the diffraction signatures. Despite the large impact parameter, the probability of an event lensed by multiple halos is still low because the Einstein radius is small, normally $10^3 - 10^4$ times smaller than the virial radius of the host halo.

According to our preliminary estimation, if CDM predominates the matter content of the universe, the chance of detecting diffraction effect by LISA is about more than 1%, regarding of the source MBH binaries within the mass range of $10^{5.0} \sim 10^{6.5} M_{\odot}$. If, on the other hand, warm DM predominates, the chance of detecting the diffraction effect would be diminished by at least one order of magnitude. Therefore, looking for the wave-optics effects in LISA events could help us constrain the DM models.

As a final remark, we note that our model of the lensing signal and the criterion of discerning the diffraction effect are based on ideal assumptions. For example, we do not consider multiple lenses along the line of sight even though we have found a relatively high lensing probability. Moreover, we have assumed that the deviation of the detected signal from the model template is solely due to gravitational lensing, while for real LISA observation, other factors, such as confusion between multiple events or inaccuracy of the waveform template, could also contribute to the deviation. We will address these caveats in a future work.

ACKNOWLEDGEMENTS

This work is supported by the National Science Foundation of China grants No 11873022, 11991053, and 11805286. X.C. is partly supported by the Strategic Priority Research Program of the Chinese Academy of Sciences, Grant No. XDB23040100 and No. XDB23010200. Y.H. is partly supported by the National Key Research and Development Program of China (No. 2020YFC2201400), and Guangdong Major Project of Basic and Applied Basic Research (Grant No. 2019B030302001). We especially thank Liang Dai at University of California, Berkeley for many insightful discussions on the theory of wave-optical lensing model and precious comments on an early version of this manuscript. We also extremely thank Xiao Guo at National Astronomical Observatories of China (NAOC) for providing us with valuable suggestions on various problems encountered in this work.

DATA AVAILABILITY

The data underlying this article will be shared on reasonable request to the corresponding author.

REFERENCES

Abbott B. P., et al., 2016, *Phys. Rev. Lett.*, 116, 131103
 Abbott B. P., et al., 2019, *Phys. Rev. X*, 9, 031040
 Abbott R., et al., 2020, arXiv e-prints, p. [arXiv:2010.14527](https://arxiv.org/abs/2010.14527)
 Amaro-Seoane P., et al., 2017, arXiv e-prints, p. [arXiv:1702.00786](https://arxiv.org/abs/1702.00786)
 Bontz R. J., Haugan M. P., 1981, *Ap&SS*, 78, 199
 Cao Z., Li L.-F., Wang Y., 2014, *Phys. Rev. D*, 90, 062003
 Christian P., Vitale S., Loeb A., 2018, *Phys. Rev. D*, 98, 103022
 Cooray A., Sheth R., 2002, *Physics Reports*, 372, 1–129
 Cusin G., Lagos M., 2020, *Phys. Rev. D*, 101, 044041
 Cutler C., Flanagan E. E., 1994, *Phys. Rev. D*, 49, 2658
 Cyranowski J. F., 1974, PhD thesis, Wisconsin Univ., Milwaukee
 Dai L., Li S.-S., Zackay B., Mao S., Lu Y., 2018, *Phys. Rev. D*, 98, 104029

Diego J. M., Hannuksela O. A., Kelly P. L., Pagano G., Broadhurst T., Kim K., Li T. G. F., Smoot G. F., 2019, *A&A*, 627, A130
 Diemand J., Moore B., Stadel J., 2004, *Monthly Notices of the Royal Astronomical Society*, 352, 535–546
 Finn L. S., 1992, *Phys. Rev. D*, 46, 5236
 Gao L., De Lucia G., White S. D. M., Jenkins A., 2004a, *Monthly Notices of the Royal Astronomical Society*, 352, L1–L5
 Gao L., White S. D. M., Jenkins A., Stoehr F., Springel V., 2004b, *Monthly Notices of the Royal Astronomical Society*, 355, 819–834
 Gil Choi H., Park C., Jung S., 2021, arXiv e-prints, p. [arXiv:2103.08618](https://arxiv.org/abs/2103.08618)
 Giocoli C., Tormen G., van den Bosch F. C., 2008, *Monthly Notices of the Royal Astronomical Society*, 386, 2135–2144
 Han J., Cole S., Frenk C. S., Jing Y., 2016, *Monthly Notices of the Royal Astronomical Society*, 457, 1208–1223
 Hannuksela O. A., Haris K., Ng K. K. Y., Kumar S., Mehta A. K., Keitel D., Li T. G. F., Ajith P., 2019, *The Astrophysical Journal*, 874, L2
 Hou S., Li P., Yu H., Biesiada M., Fan X.-L., Kawamura S., Zhu Z.-H., 2020, arXiv e-prints, p. [arXiv:2009.08116](https://arxiv.org/abs/2009.08116)
 Jung S., Shin C. S., 2019, *Phys. Rev. Lett.*, 122, 041103
 Lawrence J. K., 1971, *Nuovo Cimento B Serie*, 6B, 225
 Liao K., Biesiada M., Fan X.-L., 2019, *ApJ*, 875, 139
 Libeskind N. I., Frenk C. S., Cole S., Helly J. C., Jenkins A., Navarro J. F., Power C., 2005, *Monthly Notices of the Royal Astronomical Society*, 363, 146–152
 Lindblom L., Owen B. J., Brown D. A., 2008, *Phys. Rev. D*, 78, 124020
 Lovell M. R., Frenk C. S., Eke V. R., Jenkins A., Gao L., Theuns T., 2014, *Monthly Notices of the Royal Astronomical Society*, 439, 300–317
 Marković D., 1993, *Phys. Rev. D*, 48, 4738
 Meena A. K., Bagla J. S., 2020, *MNRAS*, 492, 1127
 Mei J., et al., 2020, *Progress of Theoretical and Experimental Physics*, 2021
 Mishra A., Meena A. K., More A., Bose S., Singh Bagla J., 2021, arXiv e-prints, p. [arXiv:2102.03946](https://arxiv.org/abs/2102.03946)
 Moylan A. J., McClelland D. E., Scott S. M., Searle A. C., Bicknell G. V., 2008, in *The Eleventh Marcel Grossmann Meeting On Recent Developments in Theoretical and Experimental General Relativity, Gravitation and Relativistic Field Theories*. pp 807–823 ([arXiv:0710.3140](https://arxiv.org/abs/0710.3140)), doi:[10.1142/9789812834300_0038](https://doi.org/10.1142/9789812834300_0038)
 Nakamura T. T., 1998, *Phys. Rev. Lett.*, 80, 1138
 Nakamura T. T., Deguchi S., 1999, *Progress of Theoretical Physics Supplement*, 133, 137
 Nitz A., et al., 2020, gwastro/pycbc: PyCBC release v1.16.11, doi:[10.5281/zenodo.4075326](https://doi.org/10.5281/zenodo.4075326), <https://doi.org/10.5281/zenodo.4075326>
 Oguri M., Takahashi R., 2020, *ApJ*, 901, 58
 Ohanian H. C., 1974, *International Journal of Theoretical Physics*, 9, 425
 Peters P. C., Mathews J., 1963, *Physical Review*, 131, 435
 Robson T., Cornish N. J., Liu C., 2019, *Classical and Quantum Gravity*, 36, 105011
 Santamaría L., et al., 2010, *Phys. Rev. D*, 82, 064016
 Schneider P., Ehlers J., Falco E. E., 1992, *Gravitational Lenses*. New York: Springer, doi:[10.1007/978-3-662-03758-4](https://doi.org/10.1007/978-3-662-03758-4)
 Sonnabend D., 1979, PhD thesis, Stanford Univ., CA.
 Takahashi R., 2004, *A&A*, 423, 787
 Takahashi R., 2006, *ApJ*, 644, 80
 Takahashi R., 2017, *ApJ*, 835, 103
 Takahashi R., Nakamura T., 2003, *ApJ*, 596, L231
 Wang J., Bose S., Frenk C. S., Gao L., Jenkins A., Springel V., White S. D. M., 2020, *Nature*, 585, 39–42
 Wang J.-S., Herrera-Martín A., Hu Y.-M., 2021, *Phys. Rev. D*, 104, 083515
 Yamamoto K., 2005, *Phys. Rev. D*, 71, 101301
 Yoo C.-M., Nakao K.-i., Kozaki H., Takahashi R., 2007, *ApJ*, 655, 691

APPENDIX A: RELATION BETWEEN HALO MASS AND LENS MASS IN THE SIS MODEL

We assume that DM halo follows an SIS density profile,

$$\rho(r) = \frac{\sigma_v^2}{2\pi G r^2}, \quad (\text{A1})$$

where σ_v is the velocity dispersion. According to this profile, the total mass of the halo, M_h , is related to the virial radius $r_{\text{vir}}(M_h, z_h)$, which is a function of the mass M_h and redshift z_h , as

$$M_h = \frac{2\sigma_v^2}{G} r_{\text{vir}}(M_h, z_h). \quad (\text{A2})$$

The lens mass is defined as the mass enclosed by a circle on the lensing plane with a radius of $\xi_0 = 4\pi\sigma_v^2 D_L D_{LS}/c^2 D_S$, which is known as the Einstein radius. To calculate the lens mass M_L , we use the surface density of an SIS projected on the lensing plane, $\Sigma(\xi) = \sigma_v^2/(2G\xi)$ (Takahashi & Nakamura 2003), and derive

$$M_L = \frac{4\pi^2\sigma_v^4 D_{LS} D_L}{G D_S c^2}. \quad (\text{A3})$$

To relate the halo mass to the lens mass, we use Equations (A2) and (A3) to eliminate σ_v and we find that

$$M_h = r_{\text{vir}}(M_h, z_h) \sqrt{\frac{M_L D_S c^2}{\pi^2 G D_{LS} D_L}}. \quad (\text{A4})$$

Figure A1 shows the relationship between these two masses and the dependence on the redshift of the halo.

This paper has been typeset from a \LaTeX file prepared by the author.

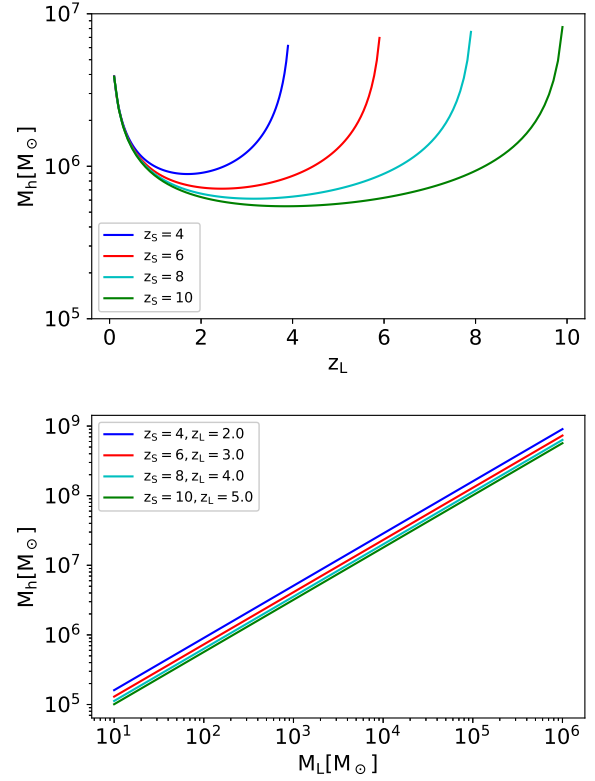


Figure A1. The upper panel shows the halo mass as a function of the redshift when the lens mass is fixed to $100 M_\odot$. Different lines correspond to different redshift of the source. The lower panel shows the halo mass as a function of lens mass M_L . Different lines correspond to different combinations of the source and lens redshifts.